Fast Green's Function Evaluation for Sources and Observers Near Smooth Convex Bodies

Yaniv Brick, Vitaliy Lomakin, and Amir Boag

***Abstract*—An efficient procedure for the evaluation of the Green's function for a source and multiple observation points near a convex impedance boundary cylinder is presented. The evaluation is performed using non-uniform grids spread along the cylinder's perimeter and regionally tailored for capturing the Green's function's behavior in the line-of-sight and shadow regions. On these grids, the Green's function is assumed to be *accurately* pre-computed using analytical or numerical techniques. The procedure is demonstrated for the circular case associated with the generalized equivalence integral equation.**

***Index Terms*—Green's function, integral equations, moment methods.**

I. Introduction

The computation of the modified Green's function (MGF) [1] for a line source near a z-invariant impenetrable object is a fundamental problem in electromagnetics. As such, it has been studied for several decades. For some particular cases, such as circular and elliptical cylinders, exact analytical solutions, in the form of a Mie series summation, were developed [2]. For more general cases of a smooth convex z-invariant cylinder, asymptotic methods such as the geometrical theory of diffraction (GTD) [3] have been employed. These provided a phenomenological solution, comprising contributions associated regionally with either direct and reflected rays, or creeping rays, in the cylinder's illuminated and shadow regions, respectively. Later works suggested uniform diffraction solutions which are also applicable near and at the cylinder' shadow boundaries [4]. However, the accuracy provided by asymptotic methods is limited and for many cases insufficient. Higher accuracy for general cases can be achieved by using numerically exact solvers based on integral equations (IE) discretized via the method of moments (MoM) [5]. The IE's solution is a surface source distribution from which the scattered component of the MGF can be computed via a field integral.

The computational cost involved with the exact methods is proportional to the problem's size. In the 2-dimensional (2D) case, for any given source-observer pair, the analytical Mie series computation involves the summation of $\mathcal{O}(N)$ terms at an $\mathcal{O}(N)$ cost ($N = \mathcal{O}(kR)$, where $2R$ is the scatterer's maximum linear dimension and k is the wavenumber). Also, if the exact MoM solution is provided for a given excitation (source location), the field integral can be evaluated at an $\mathcal{O}(N)$ computational cost per observation point. If the solution is to be computed at a large a-priori given set of $\mathcal{O}(N)$ observation points, fast field evaluation algorithms can reduce the overall cost of scattered field integrations to $\mathcal{O}(N \log N)$ (rather than $\mathcal{O}(N) \times \mathcal{O}(N)$ [6], [7]), at the expense of the accuracy's reduction. Such algorithms often rely on the asymptotic nature of free space propagation. While being capable of efficiently evaluating fields which are radiated by arbitrary shaped source distributions, they do not necessarily *optimally* capture the MGF in the presence of a convex scatterer. The general nature of these techniques leads to unnecessary computational cost which can be avoided by exploiting the asymptotic behavior of the field's propagation along the scatterer boundaries, rather than in the free space.

In this contribution, we present a technique for the efficient evaluation of the MGF for the case of a z-invariant impedance boundary cylinder. The fast evaluation is based on a coarse non-uniform sampling of the MGF along the cylinder's perimeter. The coarse sampling is allowed thanks to phase- and amplitude-compensation of the MGF using regionally computed compensation factors, which are determined by the asymptotic behavior of the propagation along the cylinder's circumference. The compensation factors in the cylinder's line-of-sight and shadow regions are specifically constructed for the reflected and creeping rays, respectively [3]. The tailored-per-region grids are designed to capture the compensated MGF (CMGF) in each of the regions at a fixed number of points, summing up to the total of $\mathcal{O}(1)$ grid points, from which the MGF can be reconstructed at any observation point, at an $\mathcal{O}(1)$ cost, via local interpolation. Hence, for a large set of $\mathcal{O}(N)$ observation points, the overall cost is of $\mathcal{O}(N)$ (rather than the $\mathcal{O}(N \log N)$ cost of the conventional fast field evaluation techniques). The algorithm allows for the computation of the MGF at a sufficient accuracy, such as that required for the numerical solution of the generalized field integral equation (GEIE) [8]. Naturally, the advantages of relying on the scattering problem's asymptotic behavior become more pronounced for geometries that are large compared to the wavelength.

II. Problem Formulation

Consider the problem of an infinite z-directed line current source $J_z = \delta(\mathbf{r} - \mathbf{r}')$ near a large smooth convex z-invariant impenetrable cylinder with a cross-section S. The electric field is z-polarized and satisfies the Helmholtz equation, in the region external to S, and an impedance (Leontovitch) boundary condition $E_z = \eta_s H_t$ on S (H_t being the magnetic field's component tangential to S). A time-harmonic dependence $e^{j\omega t}$ is assumed and suppressed. We are interested in computing the electric field $E_z(\mathbf{r})$ due to J_z in the presence of S, i.e., the MGF, at an arbitrary observation point $\mathbf{r}$ in the area surrounding S. Both $\mathbf{r}$ and $\mathbf{r}'$ lie within a proximity h from S, as depicted in Fig. 1. Using a scattering problem formulation, we write the MGF $G_m(\mathbf{r}, \mathbf{r}')$ as a sum of incident and scattered contributions, $G_i(\mathbf{r}, \mathbf{r}')$ and $G_s(\mathbf{r}, \mathbf{r}')$, respectively, such that

$$G_m(\mathbf{r}, \mathbf{r}') = G_i(\mathbf{r}, \mathbf{r}') + G_s(\mathbf{r}, \mathbf{r}'). \tag{1}$$

Here $G_i(\mathbf{r}, \mathbf{r}')$ is the free space Green's function $G_i(\mathbf{r}, \mathbf{r}') = -(k\eta/4)H_0^{(2)}(k|\mathbf{r} - \mathbf{r}'|)$ (η and $H_0^{(2)}(\cdot)$ being the intrinsic impedance and the zero-order Hankel function of the second kind, respectively). The scattered contribution $G_s(\mathbf{r}, \mathbf{r}')$ is arising due to the presence of S which is excited by the incident field $G_i(\mathbf{r}, \mathbf{r}')$. It is convenient to denote $\mathbf{r}^S(\mathbf{r})$ the point on S that is closest to $\mathbf{r}$, and $\mathbf{r}_0^S$ as the point at which S intersects the x-axis. We denote $\xi(\mathbf{r})$ the path length on S from $\mathbf{r}_0^S$ to $\mathbf{r}^S(\mathbf{r})$ ($\xi' = \xi(\mathbf{r}')$, accordingly) and $\zeta(\mathbf{r}) = |\mathbf{r} - \mathbf{r}^S(\mathbf{r})|$, as depicted in Fig. 1. The notation $G_m(\zeta, \xi, \zeta', \xi')$ for the MGF will be

Manuscript received October 31, 2013; revised March 03, 2014; accepted March 04, 2014. Date of publication March 11, 2014; date of current version May 29, 2014. This work was supported in part by the Israel Science Foundation (ISF) under Grant 1081/12, by the United States-Israel Binational Science Foundation Grant No. 2008077, by DDR&D (MAFAT) of the Israeli MOD, and by the Israeli Navy.

Y. Brick and A. Boag are with the Tel Aviv University School of Electrical Engineering, Tel Aviv, 69978, Israel (e-mail: yaniv.brick@gmail.com; boag@eng.tau.ac.il).

V. Lomakin is with the Department of Electrical and Computer Engineering, University of California, San Diego, La Jolla, CA 92093 USA (e-mail: vlomakin@eng.ucsd.edu).

Color versions of one or more of the figures in this communication are available online at http://ieeexplore.ieee.org.

Digital Object Identifier 10.1109/TAP.2014.2310460

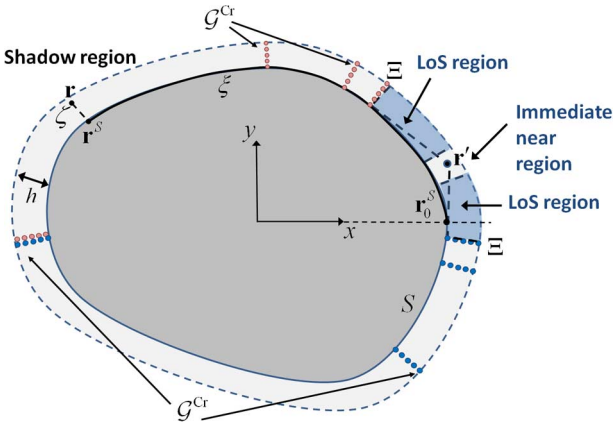

Fig. 1. The scattering problem. The source and observer are located at $\mathbf{r}'$ and $\mathbf{r}$, respectively, both within a distance of h from the scatterer's surface S. Uniform ξ-sampling of the scattered contribution is performed in the LoS region (highlighted). Beyond the LoS region, the MGF is evaluated on a non-uniform ξ-grid $\mathcal{G}^{\mathrm{Cr}}$.

occasionally used as well as similar notations for the MGF's incident and scattered contributions.

Let us assume that the solution to the scattering problem is given such that $G_{\mathrm{s}}(\mathbf{r},\mathbf{r}')$ can be computed in $\mathcal{O}(N)$ operations for a given observer $\mathbf{r}$. Since $G_{\mathrm{i}}(\mathbf{r},\mathbf{r}')$ can be computed in $\mathcal{O}(1)$ operations, an optimal evaluation scheme for the total MGF would be such that requires the direct computation of $G_{\mathrm{s}}(\mathbf{r},\mathbf{r}')$ (or $G_{\mathrm{m}}(\mathbf{r},\mathbf{r}')$) at a minimal number of points, from which the MGF over the entire domain of interest can be accurately reconstructed. The fast evaluation of the MGF, then, is performed in two stages: (a) pre-evaluation of the MGF (or its components) over a sparse set of grid points that is sufficient for reconstruction at any desired observation point, and (b) restoration of the MGF at the required observation points via local interpolations.

The coarse sampling is sufficient only if the oscillatory phase and fast amplitude decay of the MGF and its components are compensated for, prior to sampling, in a fashion detailed in the next section.

III. Efficient Sampling of the MGF

Towards the development of an efficient compensation and sampling scheme, let us first review the asymptotics of the interaction between a source and an observer near a convex cylinder. According to [3], the MGF can be described asymptotically in a manner dependent on the source and observer locations. In the case where a line of sight (LoS) exists between the two, the MGF's scattered component can be approximated by

$$G_{\mathrm{s}}(\mathbf{r},\mathbf{r}') \propto G_{\mathrm{r}}(\mathbf{r},\mathbf{r}') = \frac{\Gamma(\theta_{\mathrm{i}},\eta_{\mathrm{s}})e^{-jk(L_{\mathrm{i}}+L_{\mathrm{r}})}}{\sqrt{(L_{\mathrm{i}}+L_{\mathrm{r}}+2L_{\mathrm{i}}L_{\mathrm{r}}/(a\cos\theta_{\mathrm{i}})}} \tag{2}$$

where L_{i} and L_{r} are the distances between the specular reflection point and the source and observer points, respectively, as depicted in Fig. 2(a). Also at the reflection point, θ_{i}, a, and $\Gamma(\theta_{\mathrm{i}},\eta_{\mathrm{s}})$ are the local angle between the incident ray and the normal to the cylinder, the surface's radius of curvature, and the ray's reflection coefficient, respectively.

When there is no LoS, the scattered and incident contributions cannot be geometrically interpreted separately, and the entire MGF is asymptotically represented via the diffracted ray field, known as the creeping wave. We assume that the cylinder is large enough such that, in the region of interest, out of two possible paths from the source to the observer, one path is associated with a contribution that is dominant compared to the other. This ray path comprises two free space propagation segment of lengths s and s', and a creeping segment

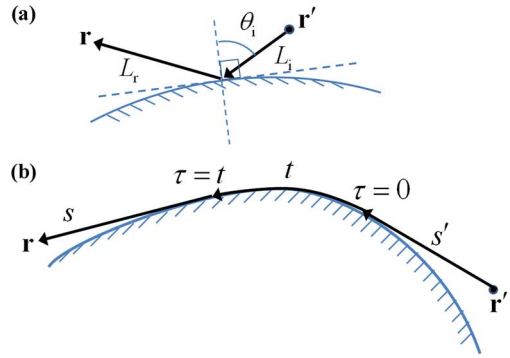

Fig. 2. (a) Specular reflection asymptotic nature of the scattered contribution in the LoS region. (b) Creeping wave asymptotic nature of the MGF in the shadow region.

of length t, as depicted in Fig. 2(b). The creeping ray contribution oscillates and decays according to

$$G_{\mathrm{m}}(\mathbf{r},\mathbf{r}') \propto \frac{1}{\sqrt{s}}\frac{1}{\sqrt{s'}}e^{-jk(s+s')}\cdot e^{-jkt-\int_0^t \alpha(\tau)d\tau}. \tag{3}$$

In (3), $1/\sqrt{s}$ and $1/\sqrt{s'}$ express the geometrical ray spreading along the free space propagation segments. The phase associated with these segments is $e^{-jk(s+s')}$. The term $\exp\{-jkt-\int_0^t \alpha(\tau)d\tau\}$ is the complex phase accumulated along the creeping segment. The integrand $\alpha(\tau)$ depends on the cylinder's radius of curvature at a coordinate τ along the creeping segment and can be computed in a manner detailed in [3].

Based on the asymptotic behavior of the interaction, we develop a region-tailored compensation, sampling, and restoration scheme. In the immediate region near the source $|\xi-\xi'| < C_{\mathrm{N}}\lambda$ (C_{N} being a constant of the order of 1) the asymptotic approximation is not valid. Hence, the scattered contribution to the MGF is computed at a uniform set of grid points $\mathcal{G}^{\mathrm{N}}$. Since this region is finite and fixed in size, the number N^{N} of points in $\mathcal{G}^{\mathrm{N}}$ is constant. From its samples $G_{\mathrm{s}}(\zeta_l,\xi_m,\zeta',\xi')$, $G_{\mathrm{s}}(\zeta,\xi,\zeta',\xi')$ is reconstructed via:

$$G_{\mathrm{s}}(\mathbf{r},\mathbf{r}') = G_{\mathrm{s}}(\zeta,\xi,\zeta',\xi') = \sum_{l,m} w_{lm}(\zeta',\xi')G_{\mathrm{s}}(\zeta_l,\xi_m,\zeta',\xi') \tag{4}$$

where w_{lm} are interpolation weights. The entire MGF is computed by adding $G_{\mathrm{i}}(\mathbf{r},\mathbf{r}')$ (which can be directly computed) to $G_{\mathrm{s}}(\mathbf{r},\mathbf{r}')$. In the regions further away from the source, the asymptotic behavior is used to design a compensation factor, which allows for a coarser sampling of either the entire MGF or its scattered contribution.

Let us define Ξ as the limit such that all the points $\mathbf{r}: |\xi-\xi'| < \Xi$ are visible to $\mathbf{r}'$. The region outside S bounded by Ξ is termed the LoS region (see Fig. 1). In the LoS region, the MGF can also be computed by the summation of a directly computed incident contribution and an interpolated scattered contribution. However, unlike in the near region, here we can use the asymptotic specular reflection behavior described by (2) to obtain a phase- and amplitude-compensated form

$$\tilde{G}_{\mathrm{s}}(\zeta,\xi,\zeta',\xi') = \tilde{G}_{\mathrm{s}}(\mathbf{r},\mathbf{r}') = G_{\mathrm{s}}(\mathbf{r},\mathbf{r}')\cdot G_{\mathrm{r}}^{-1}(\mathbf{r},\mathbf{r}'). \tag{5}$$

The compensated contribution in (5) can be reconstructed from its samples $\tilde{G}_{\mathrm{s}}(\zeta_l,\xi_m,\zeta',\xi')$ on the grid $\mathcal{G}^{\mathrm{LoS}}$ via interpolation, after which the phase and amplitude can be restored, using a factor reciprocal to that of (5), i.e., $G_{\mathrm{r}}(\mathbf{r},\mathbf{r}')$, at the observation point. The compensated contribution is smooth enough to be sampled uniformly at a fixed number of grid points.

Finally, further away from the source, in the region $|\xi-\xi'| > \Xi$, most observation points are located entirely in the "shadow region"

with respect to the source location. For these points, it is justified to use the asymptotic creeping wave term in (3) as a compensation factor, this time for the entire MGF. However, there are a few points in this region, which do have a LoS with the source and for which the term in (3) is undefined. Using a separate compensation function for these points will cause discontinuities in the MGF's compensated form. This must be avoided to allow for the MGF's reconstruction via interpolation. To that end, we simplify our compensation function to the inverse complex phase accumulated along the path on S from $\mathbf{r}^S(\mathbf{r}')$ to $\mathbf{r}^S(\mathbf{r})$

$$G_{\mathrm{c}}^{-1}(\xi,\xi') = e^{jk|\xi-\xi'|+\int_{\xi'}^{\xi}\alpha(\tau)d\tau}. \tag{6}$$

This may cause slight inaccuracies in the compensation, but allows maintaining the CMGF's continuity. (It is possible that this problem can be more accurately mitigated using a uniform GTD asymptotic term that is continuously defined in both LoS and shadow regions, including the shadow boundary. Yet, in this work we did not explore this possibility and implemented the simplified form in (6), which sufficed for the cases demonstrated later in Section V). The resulting CMGF is given by

$$\tilde{G}_{\mathrm{m}}(\zeta,\xi,\zeta',\xi') = G_{\mathrm{m}}(\zeta,\xi,\zeta',\xi')\cdot G_{\mathrm{c}}^{-1}(\xi,\xi') \tag{7}$$

and can be sampled uniformly with respect to ζ, and the reciprocal "ξ-distance" $\upsilon = 1/|\xi-\xi'|$ at fixed sampling rates. The resulting grid $\mathcal{G}^{\mathrm{Cr}}$, designed to capture the creeping wave, is non-uniform as it is denser near the sampling domain boundaries $\xi = \xi' \pm \Xi$. Since the range $0 < \upsilon < 1/\Xi$ is of a constant size, the number of the υ-sampling points N^{Cr} is also constant.

IV. The Circular Case

Let us now focus on the particular case, which serves here as a representative example, of a circular cylinder of radius a (and which is important for the GEIE application). For this configuration, $G_{\mathrm{s}}(\mathbf{r},\mathbf{r}')$ can be computed via the Mie series summation

$$G_{\mathrm{s}}(\mathbf{r},\mathbf{r}') = \sum_n e^{jn\varphi}\frac{H_n^{(2)}(k\rho)H_n^{(2)}(k\rho')J_n(ka)}{H_n^{(2)}(ka)} \cdot\frac{(\eta_s J_n'(ka)/j\eta J_n(ka)-1)}{\left(\eta_s H_n'^{(2)}(ka)/j\eta J_n(ka)-1\right)} \tag{8}$$

where $J_n(\cdot)$ and $H_n^{(2)}(\cdot)$ are the nth order Bessel and Hankel (2nd kind) functions, and $J_n'(\cdot)$ and $H_n'^{(2)}(\cdot)$ are their first derivatives, respectively. The series is truncated to include only the orders $n \in [-N_{\mathrm{Mie}} : N_{\mathrm{Mie}}]$ with $N_{\mathrm{Mie}} = \mathcal{O}(ka)$. Each computation of (8) is performed at the cost of $\mathcal{O}(N)$ operations. The radial and angular coordinates (ρ,φ) can replace the general case ones (ζ,ξ). The circular symmetry also allows us to write the interaction between $\mathbf{r}' = (\rho',\varphi')$ and $\mathbf{r} = (\rho,\varphi)$ as a function of both radii and the relative angular coordinate $\hat{\varphi} = \varphi - \varphi'$. We are interested in computing the MGF in the ring $R_{\mathrm{i}} < \rho,\rho' < R_{\mathrm{o}}$, $-\pi < \hat{\varphi} < \pi$. Just as in the general case, the ring can be divided, this time angularly, into the different observation regions. The immediate near region will be that for which $|\hat{\varphi}| < C_{\mathrm{N}}\lambda/a$. As for the LoS region, it can be defined per source point in a manner similar to that of the general case. However, assuming that $R_{\mathrm{i}} > a$, an angular limit Φ can be defined such that all the points in $\mathbf{r} : |\hat{\varphi}| < \Phi$ are visible to any source point $R_{\mathrm{i}} < \rho' < R_{\mathrm{o}}$. The shadow region can be naturally defined by $\mathbf{r} : |\hat{\varphi}| > \Phi$.

In the LoS region, the scattered contribution $G_{\mathrm{s}}(\rho,\rho',\hat{\varphi})$ can be reconstructed from its compensated form samples $\tilde{G}_{\mathrm{s}}(\rho_l,\rho_m',\hat{\varphi}_n)$. Note that the sampling in both radial coordinates results in greater savings for the case of multiple sources and observers. The phase- and amplitude-restoration coefficient remains as in (5). In the shadow region, the simplified compensation factor of (6) is reduced to

$$\tilde{G}_{\mathrm{m}}(\rho,\rho',\hat{\varphi}) = e^{jk'a|\hat{\varphi}|}G_{\mathrm{m}}(\rho,\rho',\hat{\varphi}) \tag{9}$$

where the complex phase $k'a|\hat{\varphi}|$ in $e^{jk'a|\hat{\varphi}|}$ is obtained from the creeping wave term in (6) for a constant radius of curvature a. Note the notation k' for the complex wave number associated with the creeping ray propagation. For the circular case it can be computed analytically (see [3]) such that

$$k'(a,\eta_{\mathrm{s}}) = k + \tau(ka,\eta_{\mathrm{s}})\cdot(ka)^{\frac{1}{3}}/a. \tag{10}$$

Here, $\tau(ka,\eta_s)$ is a complex coefficient associated with the first circumferential mode propagating along the cylinder's perimeter, which can be obtained by solving a trigonometric equation (detailed in [3]), given the cylinder's radius and impedance. Alternatively, using the analytical result for the perfect electric conductor (PEC) case [3], i.e.,

$$\tau_0(ka) = \tau(ka,\ \eta_{\mathrm{s}}=0) = \frac{1}{2}\left(3\pi\left(\frac{3}{4}\right)\right)^{\frac{2}{3}}e^{-j\pi/3} \tag{11}$$

the resulting $k'(a,0) = k_0'$ provides satisfactory phase compensation. The remaining inaccuracies in the amplitude compensation can be corrected based on a two-point fitting of $e^{jk_0'a|\hat{\varphi}|}G_{\mathrm{m}}$ to a function of the form $e^{-\Delta k\cdot a|\hat{\varphi}|}$, Δk being a correction to $\mathrm{Im}\{k_0'\}$.

It is worthwhile noting that (i) Since the MGF is symmetric with respect to $\hat{\varphi}$ it is sufficient to construct the positive-$\hat{\varphi}$ grids only, and (ii) the structure of the MGF in (8) allows for the evaluation at any desired set of angles based on a single grid of coefficients computed for the source and observation radii and each order of the Mie series. The circular case is convenient for implementation while it allows investigating the key features of the suggested method, as detailed in the next section.

V. Numerical Examples

We first validate the proposed phase- and amplitude-compensation scheme, using the circular case with $a = 32\lambda$ and $\eta_{\mathrm{s}} = 100\ \Omega$. A "well-compensated" MGF should have minimal variations in both phase and amplitude along the cylinder's circumference. This can also be viewed as minimization of the CMGF's spatial bandwidth. The first part in the bandwidth's reduction is achieved by an accurate phase-compensation, which practically demodulates the MGF's spectral content to the base-band. The width of the remaining spectral content around zero spatial frequency is determined by the exponential amplitude decay, and is further reduced by accurate amplitude-compensation which "flattens" the CMGF and allows for its coarse sampling.

The accuracy of the phase-compensation can be examined by computing the circumferential spectral content of the CMGF and verifying its symmetry around the zero spatial frequency. Fig. 3 presents the circumferential spectra of the MGF and CMGF computed using the circumferential wavenumber k_0' associated with the PEC case. The MGF was computed for $\rho' = a + 0.2\lambda$ along the arc $-\pi < \hat{\varphi} < \pi$, $\rho = \rho'$ (excluding $\hat{\varphi} = 0$). The circumferential spectral contents of the counter clockwise (CCW) propagating parts of G_{m} and $e^{jk_0'a|\hat{\varphi}|}G_{\mathrm{m}}$ in the shadow region were computed by taking their Fourier transforms with respect to $a\hat{\varphi}$ in the region $\pi/4 < \hat{\varphi} < 3\pi/4$. In Fig. 3, it can be seen that the $e^{jk_0'a|\hat{\varphi}|}$ factor demodulates the MGF to the base band.

Next, $e^{jk_0'a|\hat{\varphi}|}G_{\mathrm{m}}$ along the discussed arc was used to determine k'-the circumferential wavenumber that accounts for the cylinder's impedance. The accuracy of the resulting amplitude compensation can be verified by examining the CMGF's "flatness" in the shadow region. In Fig. 4, the CMGFs, computed using k_0' and k', and the free

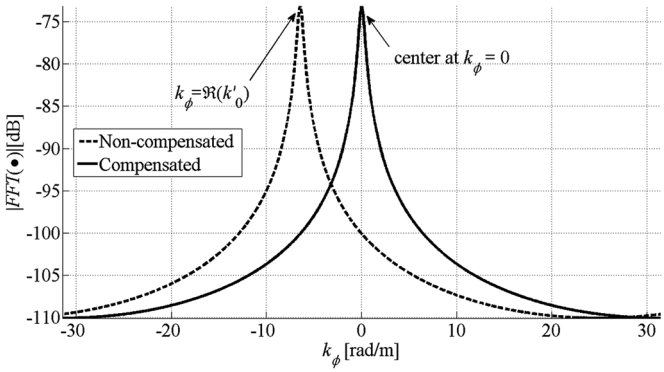

Fig. 3. Circumferential spectra of the non-compensated and compensated MGFs, $G_{\rm m}$ and $e^{jk'_0 a|\hat{\varphi}|}G_{\rm m}$, respectively. Accurate phase compensation results in demodulation to base band.

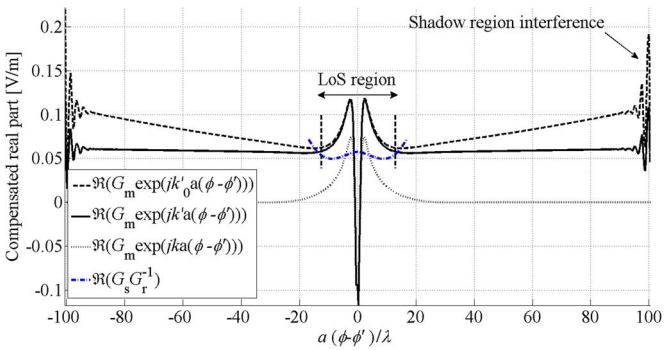

Fig. 4. Comparison of real parts of the CMGFs: $e^{jk'_0 a|\hat{\varphi}|}G_{\rm m}$, $e^{jka|\hat{\varphi}|}G_{\rm m}$, and $e^{jk'a|\hat{\varphi}|}G_{\rm m}$. Sufficient compensation is achieved outside the LoS region only. In the LoS region, $G_{\rm s}\cdot G_{\rm r}^{-1}$ is plotted.

space wavenumber k, are compared, this time for $\rho' = a + 0.4\lambda$ and $\rho = a + 0.9\lambda$. The real parts of the CMGFs are plotted. It can be seen that while using k results in an exponentially decaying CMGF and k'_0 provides slight overcompensation, the k'-CMGF is slowly varying and has an almost constant value in the shadow region, thus, allowing for its coarse sampling there. Note that for all three cases, in the LoS region (limited in this particular case by $a\Phi \approx 12.5\lambda$), the creeping wave compensation is inaccurate. There, the resulting "compensated" MGF's real part experiences a change in sign, which indicates the inaccuracy of phase-compensation, and a sharp peak indicating an amplitude-overcompensation. In contrast, the compensated *scattered* contribution in the LoS region has a slow variation behavior and does not change sign. Note also that a standing wave is formed in the deep shadow region. It is a result of the exponentially amplified interference phenomenon, and cannot be sampled as coarsely as $\tilde{G}_{\rm m}$. We avoid the insertion of error due to its under-sampling by placing the last angular sampling points in the smooth region of $\tilde{G}_{\rm m}$, and extrapolating $\tilde{G}_{\rm m}$ uniformly towards $\hat{\varphi} = \pm\pi$.

Next, we demonstrate the accuracy achieved using the proposed scheme. Our test cases involved sets of observation points on contours of the form

$$\rho(\hat{\varphi}) = R_{\rm i} + (1 + \cos(m\hat{\varphi}))\, d/2 \tag{12}$$

with $\rho' = \rho(0)$. We computed the MGF directly and via the proposed sampling and interpolation scheme, using 5th order Lagrange polynomial interpolation. The comparison is presented in Fig. 5 for the case of $R_{\rm i} = 8.25\lambda$, $d = 0.5\lambda$, $m = 12$ and $a = 8\lambda$. Also in Fig. 5, we present the absolute error computed using two different sets of grids $\{\mathcal{G}^{\rm N}, \mathcal{G}^{\rm LoS}, \mathcal{G}^{\rm Cr}\}$. The first set contained $N^{\rm N} = 7$, $N^{\rm LoS} = 6$, and $N^{\rm Cr} = 16$ angular sampling points and the second set contained twice as many points. To isolate the influence of the circumferential sampling

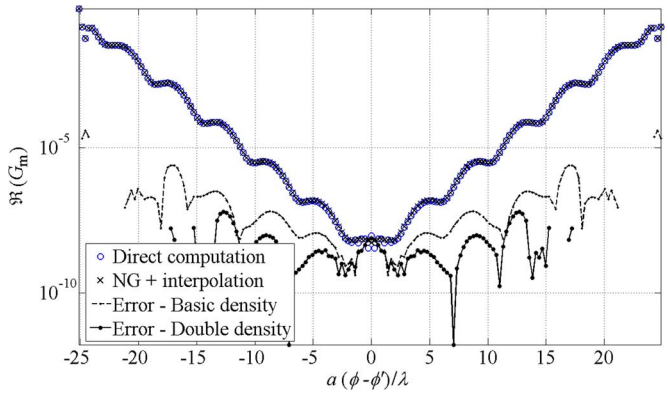

Fig. 5. Comparison of directly computed and interpolated MGF. Errors for two choices of the sampling density are presented.

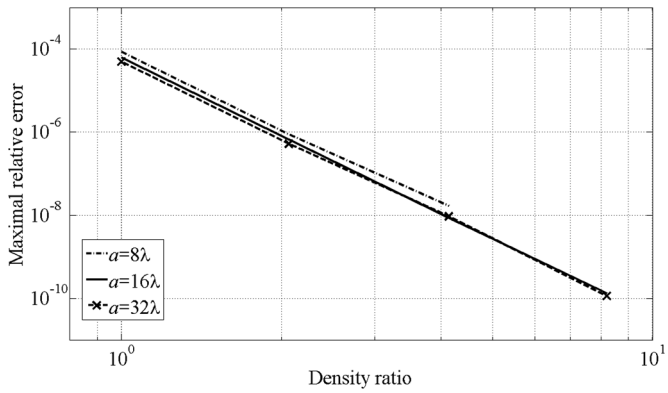

Fig. 6. Maximal error in the MGF evaluation using non-uniform sampling with a varying density ratio Ω, for three problem sizes.

on the error, both radial coordinates were excessively sampled using 50 uniformly spaced points in the range $R_{\rm i} < \rho, \rho' < R_{\rm i} + d$. The RMS and maximal relative errors for the two cases were $\varepsilon_{\rm RMS} = 1\cdot 10^{-4}$, and $\varepsilon_{\max} = 8.54\cdot 10^{-5}$, and $\varepsilon_{\rm RMS} = 1.12\cdot 10^{-6}$, $\varepsilon_{\max} = 8.8\cdot 10^{-7}$, respectively. Since the shadow region standing wave phenomenon is not captured using our sampling scheme, the relative error cannot drop below $\approx 10^{-8}$. This bound for the error is reduced exponentially (as does the phenomenon) with the problem size. Fig. 6 presents the maximal relative error obtained for $R_{\rm i} = 8\lambda$, 16λ, and 32λ, for grids obtained by multiplying the basic amounts of angular sampling points, i.e., $N^{\rm N} = 7$, $N^{\rm LoS} = 6$, and $N^{\rm Cr} = 16$, by a density ratio Ω. For all cases, increasing the sampling rates provided the error convergence expected for 5th order polynomial interpolation. It can be seen that, for each set of grid sizes, the error does not increase with the problem size, verifying that the number of sampling points is, indeed, of $\mathcal{O}(1)$ for any desired error tolerance.

VI. Conclusion

An interpolative scheme for the efficient evaluation of the modified Green's function near a smooth convex cylinder was presented. It was shown that the cost of the MGF's evaluation can be reduced to that of pre-computing its components at a fixed $\mathcal{O}(1)$ number of grid points, and interpolating it at an arbitrary observation point at an $\mathcal{O}(1)$ cost. The proposed approach is particularly efficient in cases in which the MGF is needed to be computed for multiple choices of arbitrary source and observer locations. For the circular case, even greater computational savings can be achieved thanks to the circular symmetry. For this case, the approach allows for the removal of the major computational bottleneck of repeatedly computing the MGF associated with the GEIE formulation of the scattering problem [8].

REFERENCES

[1] R. E. Collin, *Field Theory of Guided Waves*. New York, NY, USA: IEEE-Wiley, 1991, ch. 2.

[2] R. F. Harrington, *Time Harmonic Electromagnetic Fields*. Piscataway, NJ, USA: IEEE-Wiley, 2001, ch. 5.

[3] J. Keller, "Diffraction by a convex cylinder," *IEEE Trans. Antennas Propag.*, vol. 4, no. 2, July 1956.

[4] P. H. Pathak, W. D. Burnside, and R. J. Marhefka, "A uniform GTD analysis of the diffraction of electromagnetic waves by a smooth convex surface," *IEEE Trans. Antennas Propag.*, vol. 28, no. 5, pp. 631–642, Sep. 1981.

[5] A. F. Peterson, S. L. Ray, and R. Mittra, *Computational Methods for Electromagnetics*. Piscataway, NJ, USA: IEEE Press, 1998.

[6] W. C. Chew, J. M. Jin, and E. Michielssen, *Fast and Efficient Algorithms in Computational Electromagnetics*. Norwood, MA, USA: Artech House, 2001.

[7] Y. Brick and A. Boag, "Multilevel non-uniform grid algorithm for acceleration of integral equation based solvers for acoustic scattering," *IEEE Trans. Ultrason. Ferroelectr. Freq. Control*, vol. 57, no. 1, Jan. 2010.

[8] A. Boag and V. Lomakin, "Generalized equivalence integral equations," *IEEE Antennas Wireless Propag. Lett.*, vol. 11, pp. 1568–1571, 2012.

A Simultaneous Dual-Channel Micro-Radio-Repeater for Ad-Hoc Wireless Communication

Young Jun Song and Kamal Sarabandi

***Abstract*—A dual-channel subwavelength low-power radio repeater system is presented in this communication. The repeater system is composed of a low-profile miniaturized receive antenna, an end-fire two-element miniaturized transmit antenna array, and a low-power high-gain amplifier chain. The isolation between the receive antenna and transmit antenna is achieved by a near-field cancellation method. To achieve a dual-channel response antennas are made wideband using parasitic elements and the open-loop transfer function is designed in a manner to present zero-crossing phase at two frequency points within the band. The closed-loop gain of the repeater system has a gain higher than that of the amplifier at the zero-crossing phase frequency points, which gives rise to repeater performance at two distinct channels. A prototype of the repeater system operating in $2.4 \sim 2.5$ GHz with dimensions of $39.67\ \text{mm} \times 85.39\ \text{mm} \times 3.18\ \text{mm}$ is designed and fabricated. Performance of this repeater is characterized experimentally by measuring its radar cross section (RCS). Using an amplifier chain with gain of 45 dB, it is shown that dual-channel repeater exhibits RCS values of 27.7 dBsm and 26.0 dBsm at 2.42 GHz and 2.44 GHz, respectively.**

***Index Terms*—Indoor radio communication, interference suppression, mutual coupling, repeaters.**

I. INTRODUCTION

Radio repeaters have been introduced to enhance the signal coverage and radio connectivity in complex propagation environment with strong signal attenuation and multi-path and in the absence of line-of-sight between the transmitter and receiver [1]–[5]. Radio repeaters are often useful for power constrained ad-hoc communications [6]. By amplifying and retransmitting the received RF signal, the radio repeater can reestablish line-of-sight communication in a complex channel environment if the repeater is in the direct view of both the transmitter and receiver. As a result, the radio repeater promises to extend the communication range and mitigate adverse effects of multi-path communication such as deep fading effect and exorbitant path-loss. Most radio repeaters down-convert the signal, amplify and up-convert and retransmit it at a different frequency [7], [8]. This way, the adjacent transmit (Tx) and receive (Rx) antennas are isolated. Additionally, null-space projection between the Tx and Rx antennas and spatial domain filtering have been proposed to minimize the mutual coupling [9]. Such repeaters require substantial amount of power and often require a communication protocol to handle multiple channels. Destructive interference from two Tx antennas has been introduced to attenuate the signal at the Rx antenna [10]. Although significant reduction of the mutual coupling is achieved in this technique, an odd multiple of half wavelength and delicate power distribution for the Tx antennas are required. For power limited systems simplified repeaters with only few low-power components are envisioned [11]. Such a system simply includes the Tx and Rx antennas as well as a low-power high-gain RF amplifier. One practical limitation in miniaturizing the physical dimensions and complexity of the radio repeater system is the near-field mutual coupling between the Tx and Rx antennas. This coupling creates a positive feedback and limits the system performance. Due to this intrinsic feedback loop, the gain of the RF amplifier in the repeater system should be restricted in order to prevent the system from self oscillation.

In order to decrease the mutual coupling between closely spaced antennas, numerous approaches have been studied and proposed in [12]–[15]. Generally speaking, these methods achieve the suppression of the mutual coupling by modifying the current distribution on the ground plane. Although the defected ground structure (DGS) and the artificial current paths improve the isolation between adjacent antennas to some extent, these methods cause the degradation of radiation polarization and pattern. In addition to manipulating the current distribution, artificial electromagnetic structures such as metamaterial electromagnetic band-gap (EBG) structures, which modify the effective material properties have been investigated and demonstrated in [16]–[19]. By utilizing the negative effective permeability of the medium with particular resonant characteristics, these methods inhibit wave propagation within the effective medium. However, these artificial structures usually require periodic geometry and large dimensions, which are not suitable for the miniaturized subwavelength system.

Recently, a novel isolation technique utilizing near-field cancellation has been reported in [20]. In this approach, an electromagnetic null-plane is generated and utilized to suppress the mutual coupling between closely spaced antennas. As a result, a dramatic transmitter-receiver isolation has been achieved while maintaining a subwavelength dimension for the small repeater system. This miniaturized radio repeater is shown to have the ability to amplify the received RF signal by more than 50 dB without going into oscillation. The overall repeater performance is characterized by measuring the Radar Cross Section (RCS) of the repeater in the backscatter direction. The radio repeater can be considered as a transponder, which can retransmit the received RF signal. The received and retransmitted RF signals corresponds to the incident and scattered fields. Thus, the performance of the radio repeater can be evaluated through its RCS values. Calibrating the mea-

Manuscript received May 24, 2013; revised October 05, 2013; accepted February 27, 2014. Date of publication March 11, 2014; date of current version May 29, 2014. This research was supported by the U.S. Army Research Laboratory under contract W911NF and prepared through collaborative participation in the Microelectronics Center of Micro Autonomous Systems and Technology (MAST) Collaborative Technology Alliance (CTA).

The authors are with the Radiation Laboratory, Department of Electrical Engineering and Computer Science, The University of Michigan at Ann Arbor, Ann Arbor, MI 48109-2122 USA (e-mail: yjsong@umich.edu; saraband@eecs.umich.edu).

Color versions of one or more of the figures in this communication are available online at http://ieeexplore.ieee.org.

Digital Object Identifier 10.1109/TAP.2014.2310896